Geopersia 2026, 16(1): 153-170
DOI: 10.22059/geope.2025.396562.648828

RESEARCH PAPER

Application of Full Waveform Inversion in passive seismic explorations: Some practical considerations

Mohammad Hazrati kashi [1], Mohammad Tatar [1], *, Siavash Norouzi [2]

[1] International Institute of Earthquake Engineering and Seismology (IIEES), Tehran, Iran
[2] National Iranian Oil Company (NIOC), Exploration Directorate, Tehran, Iran

Received: 02 June 2025, Revised: 04 August 2025, Accepted: 26 September 2025

Abstract
Passive seismic tomography has proven to be a valuable alternative in areas where active seismic methods face significant challenges. In this study, we investigate the application of Full Waveform Inversion (FWI) – a modern, high-resolution tomographic technique – as a potential passive seismic approach for the Dehdasht embayment, Southwest, Iran. Prior to applying FWI to the real dataset from Dehdasht, we test a proposed multi-scale workflow on a synthetic model that closely resembles the study area. Through this workflow, we examine key factors affecting the FWI performance, including source and receiver configurations, presence of noise in data and inaccuracies in source location. Encouragingly, with a receiver spacing comparable to Dehdasht acquisition network and a sufficient number of sources – particularly in Vs model– we are able to reconstruct high-resolution subsurface features such as hydrocarbon trap, high-velocity bedrock and shallow syncline structure. Even with the addition of substantial level of random noise, the results demonstrate that our proposed workflow is robust and capable of producing clear subsurface tomographic image. However, simulations incorporating erroneous source locations reveal that significant source misplacement can lead to divergence and instability in FWI process. As a result, before applying FWI to the real dataset of Dehdasht, special attention must be given to source relocation or accurate source modeling. At the end, we propose a hierarchical processing workflow to ensure the convergence toward a reliable high-resolution tomographic model of the Dehdasht embayment..

Keywords: Passive Seismic Tomography, Full Waveform Inversion, Hydrocarbon Tarp, Synthetic Modeling, Dehdasht Region, Zagros.

Introduction

The application of active seismic methods is particularly challenging in geologically and tectonically complex regions, such as sub-salt and sub-basalt environments, or when exploring deep potential targets that often serve as strategic hydrocarbon reservoirs. In contrast, passive seismic methods offer a promising alternative for overcoming these challenges. The low frequency content and higher energy of passive sources allows the seismic waves to penetrate deeper into the subsurface. More importantly, the large-amplitude shear waves generated by passive sources provide valuable information about shear-wave velocity and attenuation-properties that are highly critical in exploration and characterization of hydrocarbon reservoirs (Kapotas, et al., 2003; Tselentis et al., 2007).

Encouraged by promising results reported by Kapotas et al. (2003), Tselentis et al. (2007, 2011), Nakata et al., (2015, 2016), the National Iranian Oil Company (NIOC) deployed a dense seismological network in Dehdasht embayment, located in fold and thrust belt of central Zagros,

* Corresponding author e-mail: mtatar@iiees.ac.ir

Southwestern Iran (Figure 1). The main imaging challenges in this region stem from sub-salt condition and the depth of target zone. Situated beneath the Gachsaran salt formation and trapped by a fold-and-thrust belt configuration, it is extremely challenging to apply conventional active seismic methods for imaging of Asmari formation. Additionally, the target Asmari formation is expected to lie at a depths of approximately 3-4 Km (Bordenave & Hegre, 2005; Sherkati et al., 2005). Salinas et al., (2019) provided a comprehensive description of the network design, aimed at acquiring high-quality data for a high-resolution 3D tomographic modeling. Using more than 8000 micro-earthquakes recorded by this network and a non-linear travel-time tomography technique, Shomali et al., (2018) developed a 3D V_P and V_P/V_S velocity model that revealed complex tectonic features, such as velocity anomalies, low-angle thrust faults and synclines. Riahi et al., (2021) further analyzed the ambient noise component of this dataset and successfully extracted high-frequency body and surface waves from cross-correlated noise fields. In subsequent, they planned to use P-wave arrival times from correlograms for tomographic inversion to reconstruct the shallow velocity structure in the Dehdasht area.

Despite some achievements, conventional methods in passive seismic explorations still suffers from a considerable limitation. Most notably, they are based on ray theory, which represents a high-frequency and simplified approximation of the wave equation. As a consequence, this approximation breaks down in media with heterogeneities on the order of radiated wavelength–a typical condition at passive seismic scale (Wu & Toksöz, 1987; Husen & Kissling, 2001; Spetzler & Snieder, 2004; MacEira et al., 2015).

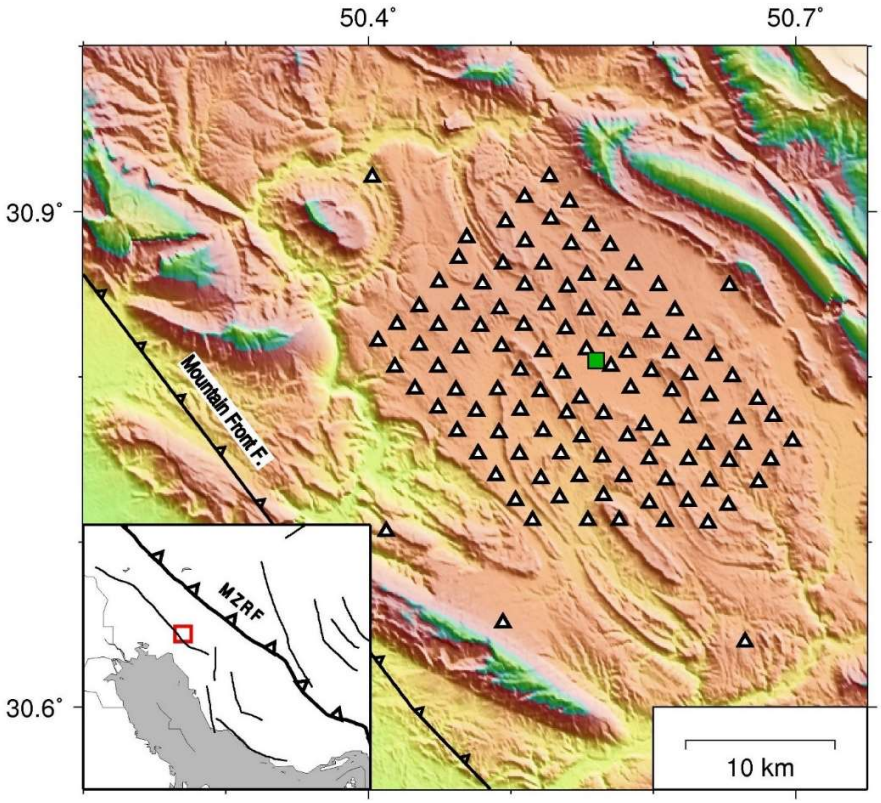

Figure 1. A topographic map of the Dehsht region featuring an inset that displays its location within Iran's Zagros fold and thrust belt (highlighted by a red rectangle). The map offers geographical context for the passive seismic network, indicated by triangles. The city of Dehdasht is marked with a green square. Seismological stations within the Dehdasht seismic network are represented by triangles. MZRF denotes the Main Zagros Reverse Fault, serving as the primary boundary between the Zagros Mountains and Central Iran

Moreover, while seismograms are rich with information from source and subsurface structures as a train of wiggles, conventional tomographic methods utilize only a small portion of this content. Travel-time tomography, for example, focuses solely on the arrival times of selected seismic phases. Consequently, this restriction in the usage of information results in a limited resolution (Claerbout, 1986; Jannane et al., 1989; Virieux et al., 2014), particularly by ignoring scattered, reflected or diffracted wavefields-which are essential for resolving fine-scale (high wavenumber) features of the subsurface.

With the advent of High Performance Computing (HPC), Full Waveform Inversion (FWI) – originally developed in the early 1980s as a recast of seismic migration (Claerbout, 1971; Claerbout & Doherty, 1972; Tarantola, 1984, 1987) – found its way into practical applications. In addition to utilizing the full information content of the seismograms, FWI explicitly incorporates the physics of seismic wave propagation into the inversion process, allowing all types of wavefields to contribute into reconstructing a high-resolution image of the subsurface. The finite-frequency nature of seismic waves is also implicitly included in the tomographic process. These significant advantages inspired us to apply this state-of-the-art technique to the unique dataset from the Dehdasht passive seismic project. However, prior to implementing FWI on the real dataset, we will first conduct a synthetic study. Our primary goals were to identify potential challenges in processing real-word data and to design an optimized workflow compatible with our passive seismic scale of interest. Furthermore, the synthetic study provides us with a valuable insight into the resolution we can expect, considering factors such as the acquisition network configuration, seismicity distribution, signal to noise ratio, number of sources included and the error in source locations. Accordingly, in this study we will first present a brief description on the synthetic model adopted for our simulations, followed by a proposed multi-scale FWI workflow for our inversion process. Given this workflow, we then assess the role of several key parameters– including receiver spacing, number of sources, noise level and source locations errors– on the inversion results.

Synthetic Model setting

To date, several synthetic models have been developed by both research and industrial institutions. Considering the challenges encountered during passive seismic data processing in Dehdasht embayment, we found the SEG/EAGE Overthrust model as a potential model to work on due to its geological and structural proximity to the Dehdasht area. A notable advantage of this model which captivated our interest the most was a hydrocarbon trap introduced between two reverse faults, in a heavily folded thrust region. Additionally, the model's dimensions (20 km×20 km×4.0 km) are large enough to approximately encompass the acquisition network of the Dehdasht passive seismic project. Although a full 3D synthetic study would be an ideal, the significant computational demands made this approach impractical. As a consequence, and in line with many prior synthetic studies, we opted for a 2D synthetic simulation on a representative section preferably passing through the hydrocarbon trap (Figure 2). For source generation, we distributed 250 random sources throughout the model with a Ricker wavelet as source time function with central frequency of 8 Hz.

Regarding the acquisition network, 78 surface stations were deployed with a spacing of 250 m. It should be mentioned that depending on the simulation purpose, we used various subsets of the available sources and receivers. Using this source-receiver configuration, we generated the synthetic seismograms from the true model to serve as the observed data. For waveform simulation, we employed the Spectral Element Method (SEM) (Komatitsch, Tromp & Sciences, 1999; Komatitsch, Ritsema & Tromp, 2002; Komatitsch et al., 2004; Tromp, Komatitsch & Liu, 2008; Peter et al., 2011), which numerically solves the elastic wave equation. Although numerical simulation of elastic waves require compressional wave velocity (V_P), shear wave

velocity (V_S) and density (Rho), but the EAGE/SEG Overthrust model only provides the V_P. To keep our synthetic study as realistic as possible, we estimated the density model using Brocher's empirical relation (Brocher, 2005) (equation 1), which is based on a diverse near-surface datasets including wireline borehole logs, vertical seismic profiles and laboratory measurements.

$$\rho(g/cm^3) = 1.4V_P^{0.25} \quad (1)$$

Additionally, analysis of existing tomography models for the Dehdasht area confirms that the conventional relation of $V_S = V_P/\sqrt{3}$ also completely holds for this area (Shomali et al., 2018; Salinas et al., 2019). Given the abovementioned considerations, we meshed the model using rectangular elements with dimensions of 100 m ×100 m and employed five Gauss-Lobatto-Legendre (GLL) points per elements in each direction. This setup ensured stable wavefield simulation up to 14 Hz.

Proposed workflow

Before initiating simulations to evaluate the role of different factors affecting the passive seismic FWI results, we first introduce our proposed workflow for this study. Consistent with prior studies, and considering the highly nonlinear nature of the FWI formulation, we adopt a hierarchical and multi-scale strategy to mitigate the nonlinearity and enhance the stability and convergence of the inversion process (Pratt, 1999; Virieux & Operto, 2009; Operto et al., 2013; Virieux et al., 2014; Ren & Liu, 2016). Within this framework, we begin the FWI process using s multi-taper traveltime difference as the misfit function, focusing on the low-frequency content of the seismograms during the initial iterations. This choice is motivated by the fact that traveltime-based misfit functions are less sensitive to uncertainties such as source magnitude, radiation pattern, attenuation model and even sensor calibration (Bozdağ, Trampert & Tromp, 2011; Tao, Grand & Niu, 2017). Moreover, traveltime information is most sensitive to the long-wavelengths components of the velocity structure, which represent the background model of the medium (Jannane et al., 1989; Huang & Schuster, 2014; Hu et al., 2018). The accuracy of this background velocity model is critical for the stability and convergence of FWI, as it determines how the high-frequency wavefields propagate throughout the medium. Furthermore, the low-frequency components of the seismograms are less prone to cycle-skipping, and the overall nonlinearity of FWI is significantly reduced at low frequencies.

As the inversion progresses and the long-wavelength structure is recovered, we gradually extend the frequency band into higher frequency ranges and switch to waveform difference misfit function in later iterations. This transition incorporates shorter-wavelength information and allows the inversion to resolve finer-scale features, effectively upgrading the background model to a high-resolution image. The complete sequence of frequency bands and corresponding misfit functions used in our multi-scale workflow is presented in table (1).

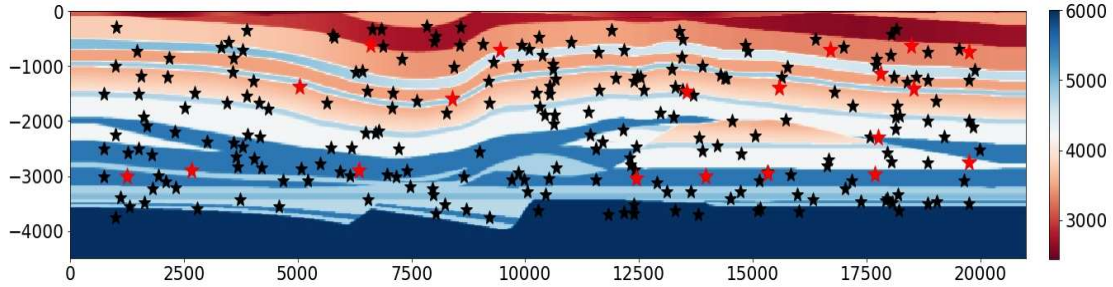

Figure 2. The 2D synthetic model of Vp used in this study. A total of 250 randomly distributed passive sources are shown across the model as black markers. Red markers indicate the subset of sources used step-length evaluation for gradient scaling described in the text

Table 1. The frequency bandwidth and misfit function used in our multi-scale FWI algorithm

Frequency band	Misfit type
0.5-1.6 Hz	Multi-taper travel time difference
0.5-2.5 Hz	Multi-taper travel time difference
0.5-2.5 Hz	Waveform difference
0.5-3.2 Hz	Waveform difference

The initial model also plays an important role in the success of the FWI. While smooth models derived from traveltime tomography are commonly employed, we adopt a more pessimistic starting point in this study–a simple 1-D vertical gradient model (Figure 3.a). This allows us to rigorously test the robustness and stability of our proposed workflow under less favorable initial conditions.

Prior to computing adjoint sources, appropriate time windows must be selected to compare the observed and synthetic seismograms and measure the misfit values. We used a hybrid approach combining manual windowing with theoretical arrival times derived from a 2D ray tracing algorithm. In addition, to equalize the impact of different event kernels and suppress unwanted instability caused by surface waves, we excluded the surface wave segments of the seismograms from the inversion process.

With adjoint sources computed, we performed adjoint simulation to obtain event kernels, which were used to calculate the gradient of the misfit function. To improve the conditioning of the inversion and ensure balanced updates across model parameters, the gradients should be preconditioned using a Hessian or an approximate Hessian operator (Virieux & Operto, 2009; Virieux et al., 2014). Accordingly, during the gradient computation and update direction estimation, each event kernel is preconditioned using an approximate Hessian operator. (Shin, Jang & Min, 2001; Rickett, 2003; Modrak & Tromp, 2016).

For model updating, a combination of Steepest Descent (SD) and the quasi-newton optimization method of limited-memory BFGS (L-BFGS; Liu & Nocedal, 1989; Byrd, Nocedal & Schnabel, 1994) are used for velocity updating. In this context, at the beginning of each frequency band or misfit function, the velocity updating is performed using steepest descent algorithm. These initial iterations provide the information about local curvature of misfit function which will be used by L-BFGS algorithm in subsequent iterations. The last remained issue concerning the model updating is the step length to take alongside the updating direction. To circumvent the computationally burdensome job of step length calculation using all sources, we used a small representative subset of the sources (red sources in Figure 2) providing adequate illumination and coverage of the model domain.

Results and Discussion

Source and receiver configuration

At the first step in our synthetic study, we assess the role of source and receiver configurations. The acquisition design is the first crucial phase in any subsurface imaging project, and understanding the resolution achievable with a specific network layout would provide valuable guidance for optimal network design. As a result, the primary goal of this analysis is to provide such insight for future passive seismic deployments aiming at subsurface imaging using FWI. To examine these effects, we tested different combinations of source and receivers. On the source side, we conducted simulations using subsets of 50, 150 and 250 randomly distributed sources. For the receivers, we evaluated spacing intervals of 250 m, 1000 m and 2000 m respectively. Notably, a spacing of 2000 m corresponds to the average receiver interval in the Dehdasht passive seismic acquisition project.

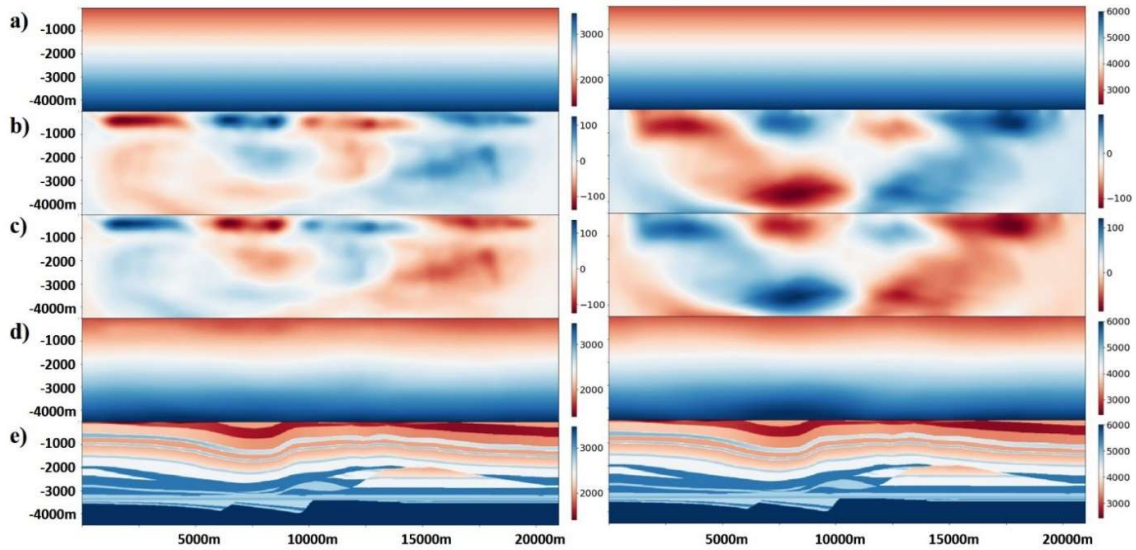

Figure 3. A comparison of velocity model updating for Vs (left panel) and Vp (right panel) at the first iteration of FWI process. a) Initial velocity models (M0). b) Misfit gradient (G). c) Update directions (-1*G). d) Updated velocity models after the first iteration (M1). e) True velocity models for comparison. This sequence illustrates the early-stage behavior of the inversion and highlights the differences in sensitivity and resolution between Vs and Vp updates

We first present the results obtained with 250 sources and 250 m receiver spacing. Figure 3 illustrates the velocity model updating process for both V_P and V_S during the first iteration of the FWI workflow. Even at this early stage, the algorithm is able to recover large-scale heterogeneities in the medium–specifically a shallow low-velocity syncline. This success is mainly due to the low-frequency content of the sources and broad illumination angle achieved via wide receiver coverage and model-wide distribution of the random sources. More interestingly and as expected, the shear-wave velocity (V_S) model captures finer structural features than the compressional-wave (V_P) model. This observation suggests that the V_S model has the potential to offer higher-resolution imaging. The workflow continues with progressive expansion of the frequency band and a switch to waveform-difference misfit function to improve resolution. Figure 4 illustrates the reduction in misfit values as the inversion progresses, with noticeable jumps corresponding to the extension of the frequency band. Extending the frequency band initially increase sensitivity to finer-scale features but also temporarily elevate the misfit due to their higher sensitivity to modeling inaccuracies. These jumps are expected in multi-scale FWI and demonstrate the algorithm's capacity to refine structural details as the inversion proceeds to shorter wavelengths. Similarly, Figure 5 shows the evolution of the V_S and V_P models across iterations. The final V_S model proves particularly effective in delineating important subsurface features, including the shallow low-velocity syncline and high-velocity bedrock. Most notably, the hydrocarbon trap is distinctly identifiable as a low-velocity anomaly within the depth range of 2000-3000m. If we want to take a step further, the algorithm shows some ability to reconstruct stratigraphic layering–a prominent advantage that aligns with the objectives of high-resolution active seismic imaging. This is noteworthy given that the main goal of Dehdasht passive seismic project is to map the subsurface topography of Asmari formation (Salinas et al., 2019). From a data-space perspective, Figure 6 demonstrate how the waveform fitness between observed and synthetic seismograms improves across iterations and frequency bands.

Considering the above configuration as a benchmark, we next evaluated scenarios that more closely reflect the limitations of the Dehdasht acquisition. Accordingly, the following configurations were tested:

$N_{sources}$= 50, $N_{receiver}$=10 , Receiver spacing=2 km
$N_{sources}$= 150, $N_{receiver}$=10 , Receiver spacing=2 km
$N_{sources}$= 250, $N_{receiver}$=10 , Receiver spacing=2 km
$N_{sources}$= 250, $N_{receiver}$=20 , Receiver spacing=1 km

The same workflow described above is applied to these alternative acquisition parameters. Surprisingly, the results indicates that even with significantly increased receiver spacing, most of the key subsurface features can still be successfully reconstructed. For a better illustration, Figures 7 and 8 compares final recovered Vp and Vs models across different acquisition configurations and at low and high frequency bands. As expected, the V_S model consistently reveal more structural detail than the Vp models, further emphasizing the superior resolution capability of shear-wave imaging. Such a promising results support the feasibility of achieving high-resolution results even with average receiver spacing as long as 2 km. This is largely due to the compensatory effect of increasing the number of sources in the inversion. Specifically, while a sparse set of sources (e.g., 50 events) may be sufficient to recover long-wavelength components or background velocity, reconstructing shorter-wavelength features demands a denser source distribution. This is because a larger number of sources improves angular illumination, thereby increasing the wavenumber coverage and enhancing the inversion's sensitivity to fine-scale structures.

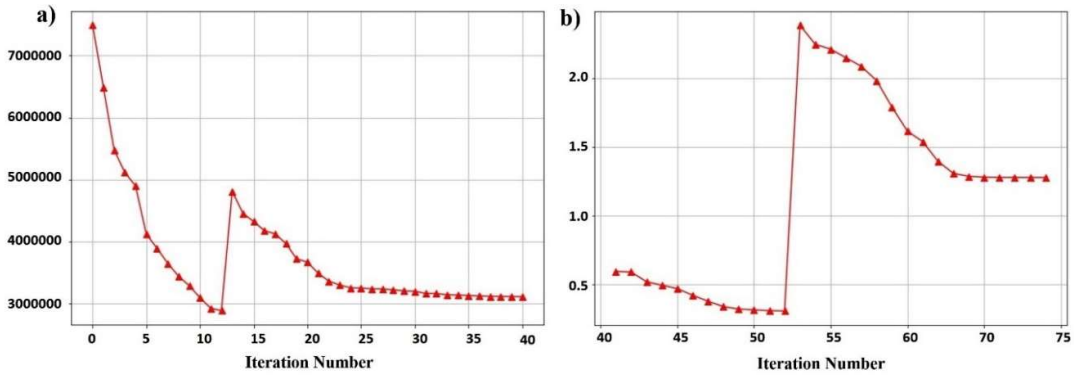

Figure 4. Misfit variations through inversion iterations for Multi-taper Travel-time Difference (a) and Waveform Difference (b) misfit functions. The jump in misfit value is due to frequency band expansion

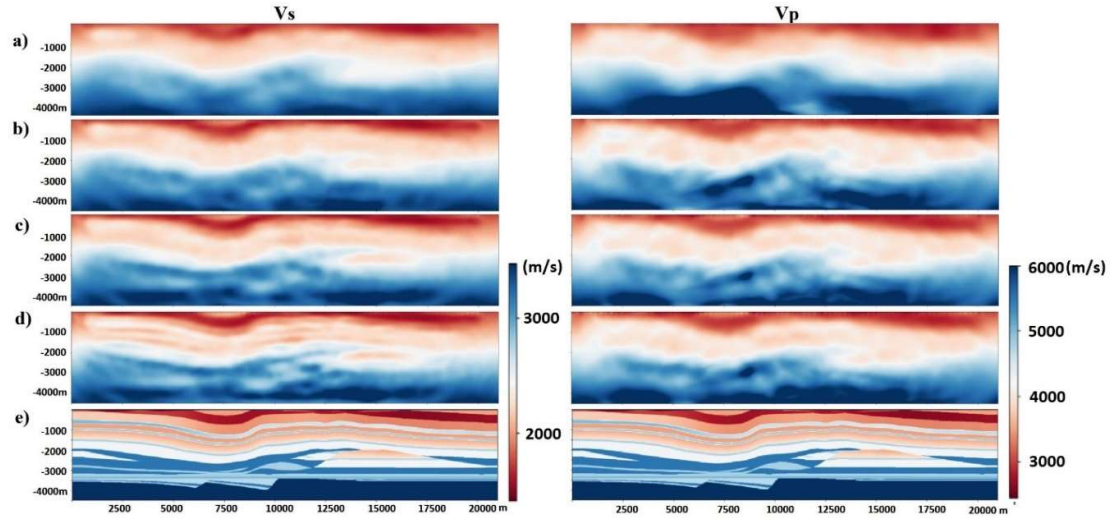

Figure 5. Reconstructed velocity models of Vs (left panel) and Vp (right panel) at different iterations of M12 (a), M40 (b), M52 (c) and M69 (d) of FWI workflow. For a better comparison, (e) the true velocity models are presented at the bottom

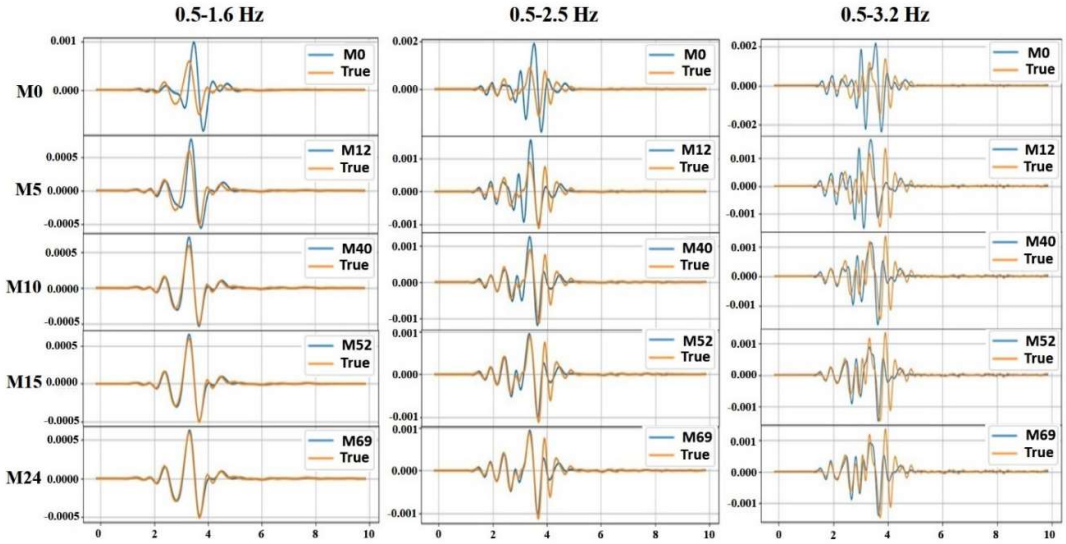

Figure 6. Waveform fitness between observed (orange) and synthetic (blue) seismograms at the frequency bands of 0.5-1.6 Hz (left), 0.5-2.5 Hz (middle) and 0.5-3.2 Hz (right) and for different iterations of M0 (initial model), M12, M40, M52 and M69 of FWI process as illustrated at Figure 5 and for a sample source and receiver

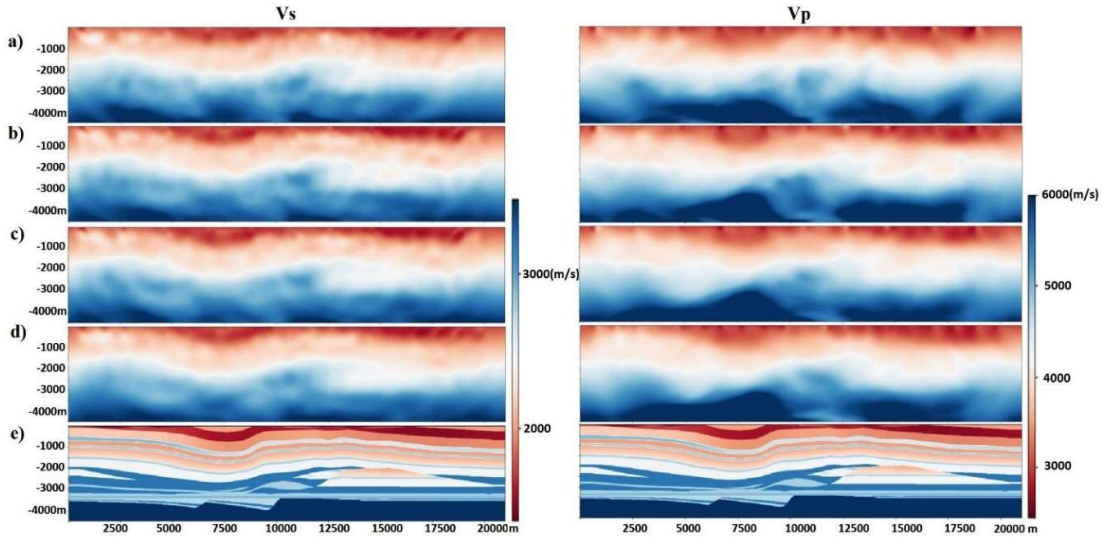

Figure 7. A comparison of obtained velocity models of Vs (left panel) and Vp (right panel) at the frequency band of 0.5-1.6 Hz and for a dataset recorded by different acquisition configurations. a) 50 sources recorded by 10 receivers (receiver spacing: 2 km). b) 150 sources recorded by 10 receivers (receiver spacing: 2 km). c) 250 sources recorded by 10 receivers (receiver spacing: 2 km). d) 250 sources recorded by 20 receivers (receiver spacing: 1 km). e) True velocity models

These findings are consistent with wave-equation theory, which states that FWI resolution is governed by wavenumber coverage, determined by the angular separation of source–receiver pairs. The wavenumber vector sampled by a given pair is proportional to:

$$\mathbf{k} \propto \frac{\omega}{v}(\hat{\mathbf{s}} + \hat{\mathbf{r}}) \quad (2)$$

where ω is the angular frequency, v is the wave velocity, and $\hat{\mathbf{s}}$, $\hat{\mathbf{r}}$ unit vectors pointing toward the source and receiver, respectively (Wu & Toksöz, 1987; Virieux & Operto, 2009). Broader angular coverage enables access to higher wavenumbers, which directly translates into improved model resolution.

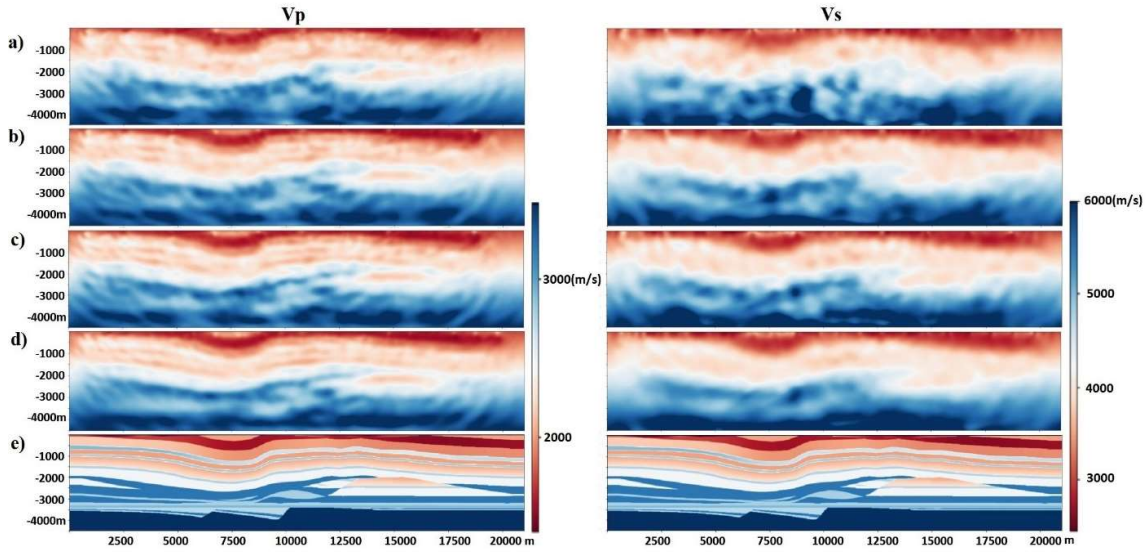

Figure 8. A comparison of obtained velocity models of Vs (left panel) and Vp (right panel) at the frequency band of 0.5-3.2 Hz and for a dataset recorded by different acquisition configurations. a) 50 sources recorded by 10 receivers (receiver spacing: 2 km). b) 150 sources recorded by 10 receivers (receiver spacing: 2 km). c) 250 sources recorded by 10 receivers (receiver spacing: 2 km). d) 250 sources recorded by 20 receivers (receiver spacing: 1 km). e) True velocity models

Receiver spacing also plays a critical role in resolving short-wavelength features. According to the spatial Nyquist criterion, the receiver interval Δx must satisfy:

$$\Delta x < \frac{v}{2f_{max}} \quad (3)$$

where f_{max} is the maximum frequency used in the inversion (Sirgue & Pratt, 2004). In our setup, with $v \approx 3000$ m/s and $f_{max} = 3.2$ Hz, the Nyquist spacing is approximately 470 m. Receiver intervals beyond this limit, such as 2 km, risk spatial aliasing and degradation of high-frequency information. Nevertheless, increasing the number of sources introduces more ray paths with diverse angles, enhancing wavenumber sampling and partially compensating for the sparse receiver network (Operto et al., 2013; Brossier et al., 2009).

In addition, the model geometry enhance the illumination power in specific regions. For example, strong reflectors such as earth's surface or high-velocity basement at the base of the model act as secondary sources, enriching wavenumber coverage for the targets located between them, such as hydrocarbon trap or syncline structure.

Extending the frequency band is another means of improving resolution. Higher frequencies yield shorter wavelengths that interact with smaller-scale features in the model, increasing the inversion's sensitivity to those features. However, taking advantage of higher frequency wavefields requires finer spatial discretization (meshing) and either denser receiver arrays or more numerous sources. These demands result in greater computational cost, including increased simulation time and memory usage–often beyond practical limits. A comprehensive study by Huang & Schuster (2014) explored the resolution limits of wave-equation-based imaging methods such as Reverse Time Migration (RTM), Least Square Migration (LSM) and FWI. Their findings indicate that multiples contain useful information about some low- and intermediate-wavenumber components of the velocity model–components that may not be recovered by primary reflections alone. Even more compelling, diffracted waves were shown to provide up to twice the resolution of primaries. Collectively, these advantages underscore the fundamental strengths of FWI over conventional tomographic techniques, particularly in scenarios where acquisition geometry is suboptimal or constrained.

Noisy Data

In this section, we assess the impact of noisy data on the inversion results. To simulate the realistic conditions, we added a white noise to each seismogram, with a standard deviation set to 20% of maximum absolute value of original seismogram. These corrupted waveforms were then treated as the observed data. Regarding the choice of 20% noise level, this value was selected based on its widespread use in synthetic inversion experiments aimed at testing algorithm robustness under moderate-to-high noise conditions (e.g., Brossier et al., 2009; Métivier et al., 2016). Several FWI studies introduce white Gaussian noise at levels ranging from 5% to 30% of the maximum trace amplitude to explore algorithm stability, misfit behavior, and noise suppression mechanisms. The 20% threshold represents a compromise: it is sufficiently high to simulate realistic passive seismic conditions (which often suffer from poor signal-to-noise ratio), yet low enough to prevent overwhelming the signal content entirely, thus enabling meaningful interpretation of model recovery performance. A broader sensitivity analysis could further strengthen the findings by quantifying inversion performance under varying noise levels (e.g., 5%, 10%, 20%, 30%), as demonstrated in prior FWI benchmarking studies (e.g., Esser et al., 2016; Tape et al., 2010). However, such an analysis was beyond the scope of this study due to the high computational cost of elastic FWI simulations, which require repeated wavefield propagations, gradient calculations, and multi-scale iterations.

The inversion results at various iterations are shown in Figure 9. Despite the introduction of substantial noise, the inversion remains surprisingly robust and successfully reconstructs the key heterogeneous features of the subsurface. This resilience can be attributed, in part, to the nature of the added noise. Since white noise applied to each seismogram is uncorrelated with the noise in other seismograms, it introduces non-coherent, uncorrelated perturbations. Such noise lacks spatial consistency across seismograms, making it more easily distinguishable from coherent signal energy and thus more effectively attenuated during the inversion process. This phenomenon is analogous to the stacking process in active seismic data processing, where random noise tends to be canceled out and the coherent signal reinforced. Similarly, in FWI, the random noise related artifacts in individual event kernels tend to cancel out during kernel summation process, the coherent structural information to dominate and emerge in the final model.

In practical scenarios, however, the ambient seismic noise is often originates from unevenly distributed sources and can exhibit coherent characteristics. These coherent noise components may resemble legitimate signal and produce strong adjoint wavefields during inversion. The seismic wavefields resulted from these sources could be mistaken for coherent signal. As a consequence, their interaction with the forward wavefield can lead to spurious artifacts in the reconstructed model. This highlights the importance of understanding the spatial and spectral properties of the background noise field.

The frequency content of the ambient noise is particularly critical, as it directly influences the frequency band suitable for inversion. Performing FWI at frequencies with poor signal-to-noise ratios may degrade the model. Therefore, analyzing the noise characteristics using power spectral density (PSD) estimates – as proposed by McNamara & Buland (2004) and McNamara et al., (2009) – can guide the selection of optimal frequency bands. This ensures that the inversion operates in a regime where the coherent signal dominates over noise, thereby improving stability and resolution.

Erroneous locations

One of the most critical challenges in the applying FWI to passive seismic data in the Dehdasht region is the uncertainty associated with earthquake source locations. To evaluate the impact of such errors, we conducted a controlled experiment in which random perturbations were

introduced into the true event coordinates. Specifically, Gaussian noise with standard deviations of 500 m in the horizontal (x) direction and 700 m in depth (z) was added to each source location. These perturbation values were chosen to reflect realistic location uncertainties expected in passive seismic networks with 2 km receiver spacing. In such configurations, typical horizontal location errors range from 350–600 m due to limited azimuthal coverage and arrival-time uncertainties of ~0.05–0.1 s and average velocity of 4.5 km/s (Kissling et al., 1994). Vertical errors are commonly 1.5–2 times larger, as surface-only arrays poorly constrain depth due to lack of steep-angle raypaths and vertical sensitivity (Kissling et al., 1994). Figure 10 compares the true (black) and perturbed (green) source locations.

To mitigate the effect of erroneous locations on the inversion, we applied a simple time-windowing scheme: adjoint source were not computed for time windows where the time shift between synthetic and observed seismogram exceeded a threshold of 0.18 s. This approach acts as an automatic screening mechanism, suppressing the influence of events with large timing discrepancies that likely result from location errors.

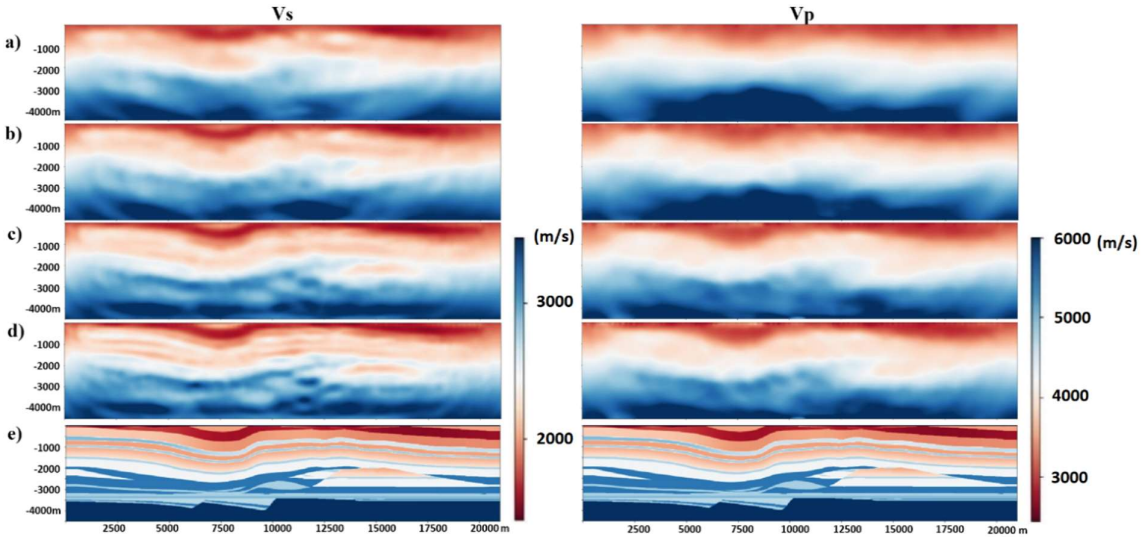

Figure 9. Reconstructed velocity models of Vs (left panel) and Vp (right panel) for noisy data at different iterations of FWI process. a) Velocity model obtained at the frequency band of 0.5-1.6 Hz and using multi-taper traveltime difference as misfit function after 9 iterations (M9). b) Velocity model obtained at the frequency band of 0.5-2.5 Hz and using multi-taper traveltime difference as misfit function after 26 iterations (M26). c) Velocity model obtained at the frequency band of 0.5-2.5 Hz and using waveform difference as misfit function after 46 iterations (M46). d) Velocity model obtained at the frequency band of 0.5-3.2 Hz and using waveform difference as misfit function after 55 iterations (M55). e) True velocity models

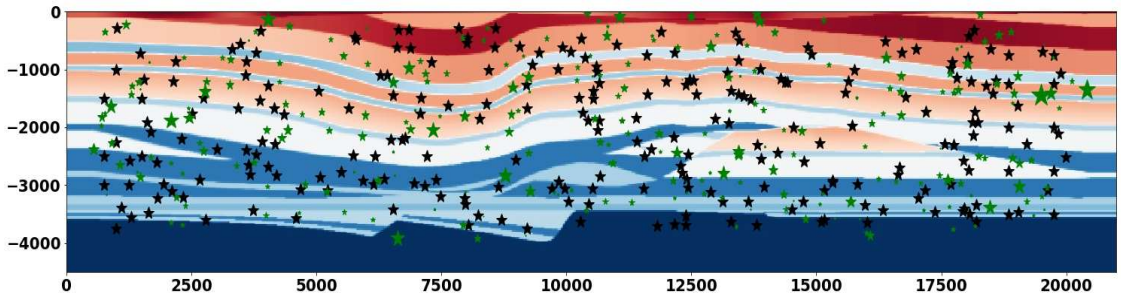

Figure 10. Spatial distribution of Erroneous locations (green) and the True source locations (black) throughout the model. The size of the markers for erroneous locations reflects the magnitude of the distance errors, with larger markers representing greater errors

Despite this strategy, the inversion proved to be highly sensitive to mislocated sources. As shown in Figure 11, the resulting Vp model reveals only vague structural impressions–such as a faint indication of the syncline and some disorganized patches of low-velocity zones–while the Vs model fails to recover any coherent structure because of two reasons. First, the lower velocity of shear waves amplifies errors induced by location uncertainties; for the same spatial mislocation, arrival-time errors are larger for Vs than Vp, leading to greater waveform mismatch. Second, the shorter wavelengths associated with shear waves increase the likelihood of destructive interference between forward and adjoint wavefields during gradient computation. Together, these effects diminish the sensitivity of the inversion to true subsurface structure and significantly impair model reconstruction in the presence of source mislocation.

A further complication introduced by source mislocation lies in the time windowing process used for adjoint source calculation. As noted earlier, the inversion focuses on the body wave portion of the seismogram–bounded by the arrivals of key seismic phases (primarily P and S) and surface wave arrival estimated by average group velocity. Errors in the source position can cause these arrival windows to be incorrectly applied, leading to the inclusion of unwanted surface-wave energy or the misalignment of S- and P-wave phases, a classic cause of cycle skipping in FWI. Such misalignments severely corrupt the adjoint source term and thus distort the model update direction.

A detailed inspection of event kernels provides a good insight into the extent of these effects. For example, Figures 12.a and 12.b compare the event kernels from a true and erroneous source locations with the highest location error. In the true source kernel, a coherent low-velocity signature outlining the syncline (highlighted by dashed box) is visible in Vp kernel. In contrast, the kernel for the erroneous source lacks any meaningful structural information and show random high-gradient noise. However, the good news is that the magnitude of erroneous kernel is much smaller (nearly 10 times) than its true-source counterpart, suggesting that the inversion is, to some extent, naturally suppressing the influence of severely mislocated source. Interestingly, in this case, the erroneous source was located shallower than the true event, resulting in systematically earlier arrivals in the synthetic waveforms. This behavior is expected from basic travel-time physics, where a shorter vertical propagation path from a shallower source leads to reduced arrival times at the receivers (Tape et al., 2010).

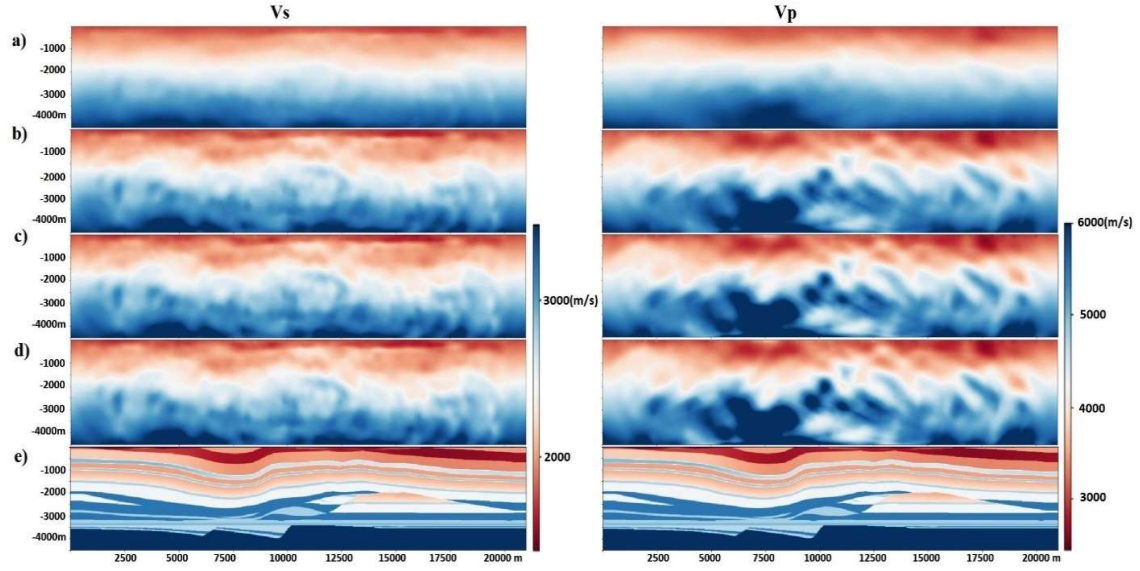

Figure 11. Reconstructed velocity models of Vs (left panel) and Vp (right panel) in the presence of source mislocation at different iterations of M5 (a), M10 (b), M15 (c), M20 (d). e) True velocity models

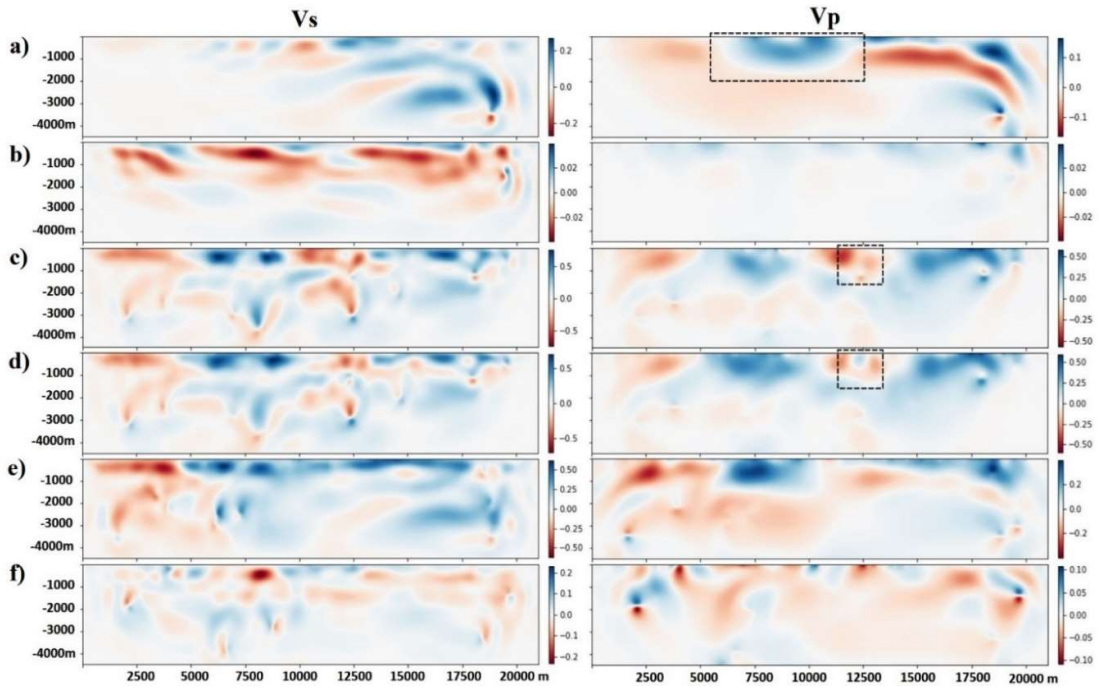

Figure 12. Analysis of event kernels for Vs (left) and Vp (right) for different situations of true and erroneous source locations at the first iteration. a,b) Event kernels associated with the true and erroneous location for the source with highest location error. c,d) Summation of event kernels associated with the true and erroneous locations for 10 sources with the lowest location errors. e,f) Summation event kernels associated with the true and erroneous locations for 10 sources with the highest location errors

When the inversion assumes the incorrect source position to be accurate, it interprets these early arrivals as being caused by overly fast wave speeds. Consequently, the algorithm compensates by introducing spurious low-velocity anomalies beneath the receiver array and surrounding the mislocated source in an attempt to delay the synthetic arrivals and reduce the misfit (Virieux & Operto, 2009; Ma & Hale, 2013). These artificial features are not representative of the true subsurface and often appear as fringe-like or lens-shaped artifacts in the resulting misfit and sensitivity kernels. Such patterns are characteristic of waveform inversion attempts to reconcile phase misalignments caused by source mislocation, especially in early iterations where gradients are dominated by travel-time information (Fichtner, 2011; Brossier et al., 2010). These kernel anomalies are especially pronounced in the near-surface, where the sensitivity to timing errors is highest, and can persist in final models if not properly mitigated through accurate relocation or joint inversion approaches.

To assess the cumulative effect of source mislocation, Figures 12.c to 12.f compare the summed misfit kernels for two source groups: the 10 events with the highest and lowest location errors. As seen in Figure 12.c and Figure 12.d the kernel for well-located events closely resembles the true structural kernel, preserving key features such as low-velocity zones between shallow sources and receivers. A localized artifact–highlighted by a dashed box –illustrates how even small depth errors can induce compensatory low-velocity anomalies.

In contrast, the kernel for the 10 most mislocated sources (Figures 12.f) bears little resemblance to the true structure (Figures 12.e) and is dominated by high-amplitude, source-centered anomalies. These artifacts risk corrupting the constructive contributions from more reliable sources when summed during inversion, further degrading the final model.

In conclusion, these results demonstrate that source mislocation is one of the most destructive factors in passive-source FWI. It can lead to the suppression of valid structural signals, the introduction of spurious anomalies, and–in extreme cases–divergence of the inversion. This

underscores the critical importance of accurate source relocation, ideally based on high-quality velocity models and advanced location methods, prior to implementing waveform inversion on passive seismic datasets.

Conclusion

In this study, we evaluated the feasibility of applying Full Waveform Inversion (FWI) to passive seismic data by conducting a series of controlled synthetic experiments designed to reflect the acquisition and geological conditions of the Dehdasht region. A multi-scale inversion workflow was proposed and tested, emphasizing its robustness against practical challenges commonly encountered in passive-source tomography.

Our results demonstrate that, despite the challenges imposed by sparse acquisition geometry and the uneven illumination typical of passive seismic deployments, Full Waveform Inversion (FWI) is capable of reconstructing key structural features of the subsurface. These include the shallow syncline, the high-velocity crystalline basement, and a prominent low-velocity anomaly interpreted as a hydrocarbon-bearing zone. The shear-wave velocity (Vs) models, in particular, consistently reveal finer-scale details than their P-wave (Vp) counterparts. This improvement stems from the inherently shorter wavelengths of shear waves at a given frequency and their heightened sensitivity to rigidity contrasts, making them more responsive to lithological variations and stratigraphic interfaces. Additionally, Vs is generally less affected by pore fluid content, which contributes to a sharper structural image.

The joint availability of Vp and Vs models also facilitates the computation of the Vp/Vs ratio, a valuable diagnostic for identifying gas-saturated zones, assessing lithofacies, and estimating rock properties such as Poisson's ratio and bulk modulus. As such, the simultaneous recovery of both Vp and Vs fields enhances not only structural interpretation but also reservoir characterization, highlighting the added value of FWI in integrated passive seismic studies.

The key findings from the synthetic simulations include:

Acquisition Network: The experiments show that increasing the number of sources significantly improves model resolution, especially under sparse receiver coverage. With average receiver spacing up to 2 km, long-wavelength features can still be accurately recovered if sufficient source illumination is achieved. Even in the worst-case scenario, the resulting model could serve as a valuable background velocity model for active seismic imaging.

Noise Robustness: The inversion process remained remarkably stable even with the introduction of strong random noise. This resilience stems from the incoherent nature of white noise, which is effectively attenuated during kernel summation. However, because ambient noise in real scenarios is often temporally and spatially coherent, future studies should incorporate more realistic noise conditions to assess FWI's true performance limits.

Source Mislocation Effects: Among all tested variables, errors in source location had the most detrimental impact. Mislocated sources caused arrival-time mismatches that the inversion erroneously corrected by introducing artificial low-velocity anomalies around receivers and sources, leading to instability and convergence failure–particularly in the Vs model. This emphasizes the critical need for reliable source relocation as a prerequisite for successful passive FWI. Given the interdependence between accurate source modeling and velocity estimation, a hierarchical strategy is required.

As a practical recommendation, we propose a staged inversion approach for the real Dehdasht dataset: beginning with 1D velocity modeling constrained by active seismic lines, followed by joint inversion for 3D velocity and source parameters using ray-based techniques (e.g., Heimann et al., 2018a,b; Lei et al., 2020; Cesca et al., 2021). The final stage would then apply full-waveform methods to iteratively refine both the velocity and source models (Liu et al., 2004, 2022; Tape et al., 2009; Lee et al., 2014). To ensure internal consistency, source

relocation should be repeated after several iterations of FWI when a more accurate velocity model becomes available.

In summary, this study confirms the strong potential of FWI in passive seismic imaging when combined with a robust workflow and careful data conditioning. The synthetic experiments provide both validation and guidance for real-data implementation in the Dehdasht passive seismic project.

Acknowledgment

This research was supported by the International Institute of Earthquake Engineering and Seismology (IIEES) under research project number 5406-748. The authors gratefully acknowledge the Exploration Directorate of the National Iranian Oil Company (NIOC) and Kish Petroleum Engineering (KPE) for providing access to high-performance computing facilities. Their support substantially reduced computation time and memory usage, enabling comprehensive simulations and robust analysis in this work. We specially appreciate two anonymous reviewers for their constructive comments and the Editor-in-Chief, Dr. Ali Kananian, for handling the manuscript. During the course of this research, SPECFEM2D and CREWS software were used for elastic wave simulations and for ray tracing, respectively. We kindly acknowledge the developer of both softwares.

Statements & Declarations:

Funding

The authors declare that no funds, grants, or other support were received during the preparation of this manuscript.

Conflict of Interests

The authors have no relevant financial or non-financial interests to disclose.

Author Contributions

Conceptualization: M. Hazrati Kashi, M. Tatar. Methodology: M. Hazrati Kashi, M. Tatar, S. Norouzi. Material preparation, data collection and analysis: M. Hazrati Kashi. Writing original draft: M. Hazrati Kashi, M. Tatar. Writing Review and Edditing: M. Hazrati Kashi, M. Tatar, S. Norouzi. Supervision: M. Tatar.

Data availability

The datasets generated during and/or analysed during the current study are available from M. Hazrati Kashi upon request (m.hazrati.kashi@gmail.com)

References

Bordenave, M. L., Hegre, J. A., 2005. The influence of tectonics on the entrapment of oil in the dezful embayment, zagros foldbelt, iran. Journal of Petroleum Geology, 28(4): 339-368.

Bozdağ, E., Trampert, J., Tromp, J., 2011. Misfit functions for full waveform inversion based on instantaneous phase and envelope measurements. Geophysical Journal International, 185(2): 845-870.

Brocher, T. M., 2005. Empirical relations between elastic wavespeeds and density in the Earth's crust, Bulletin of the Seismological Society of America. 95(6): 2081-2092.

Brossier, R., Operto, S., Virieux, J., 2009. Seismic imaging of complex onshore structures by 2D elastic frequency-domain full-waveform inversion. Geophysics, 74(6): 105-118.

Brossier, R., Operto, S., Virieux, J., 2010. Which data residual norm for robust elastic frequency-domain full waveform inversion? Geophysics. 75(3): R37-R46.

Byrd, R. H., Nocedal, J., Schnabel, R. B., 1994. Representations of quasi-Newton matrices and their use in limited memory methods. Mathematical Programming, 63(1-3): 129-156.

Cesca, S., Stich, D., Grigoli, F., Vuan, A., Lopez-Comino, J. A., Niemz, P., Blanch, E., Torsten, D., Ellsworth, W. L., 2021. Seismicity at the Castor gas reservoir driven by pore pressure diffusion and asperities loading. Nature Communications, 12(1): 4783.

Claerbout, J. F., 1971. Toward a unified theory of reflector mapping. Geophysics. Society of Exploration Geophysicists, 36(3): 467-481.

Claerbout, J. F., 1986. Imaging the Earth's Interior. Geophysical Journal of the Royal Astronomical Society. Oxford Academic, 86(1): 217-217.

Claerbout, J. F., Doherty, S. M., 1972. Downward Continuation of Moveout-Corrected Seismograms. Geophysics: 741-768.

Esser, E., Guasch, L., van Leeuwen, T., Aravkin, A. Y., Herrmann, F. J., 2016. Total Variation Regularization Strategies in Full-Waveform Inversion. SIAM Journal on Imaging Sciences, 11(1): 376-406

Fichtner, A., Trampert, J., 2011. Hessian kernels of seismic data functionals based upon adjoint techniques. Geophysical Journal International. 185(2): 775-798.

Heimann, S., Isken, M., Kühn, D., Sudhaus, H., Steinberg, A., Daout, S., Cesca, S., Vasyura-Bathke, H., Dahm, T., 2018a. Grond-A probabilistic earthquake source inversion framework. *V. 1.0. GFZ Data Services*.

Heimann, S., Cesca, S., Kühn, D., 2018b. Probabilistic moment tensor inversion for hydrocarbon-induced seismicity in the Groningen gas field, the Netherlands, part 2: Application. Bulletin of the Seismological Society of America, 110(5): 2112-2123

Hu, W., Chen, J., Liu, J., Abubakar, A., 2018. Retrieving Low Wavenumber Information in FWI: An Overview of the Cycle-Skipping Phenomenon and Solutions. IEEE Signal Processing Magazine, 35(2): 132-141.

Huang, Y., Schuster, G. T., 2014. 'Resolution limits for wave equation imaging. Journal of Applied Geophysics. Elsevier B.V., 107: 137-148.

Husen, S., Kissling, E., 2001. Local earthquake tomography between rays and waves: Fat ray tomography. Physics of the Earth and Planetary Interiors, 125(1-4): 171-191.

Jannane, M., Beydount, W., Crase, E., Cao, D., Koren, Z., Landa, E., Memdes, M., et al., 1989. Wavelengths of earth structures that can be resolved from seismic reflection data. Geophysics, 54(7): 906-910.

Kapotas, S., Tselentis, G. A., Martakis, N., 2003. Case study in NW Greece of passive seismic tomography: A new tool for hydrocarbon exploration. First Break, 21(12): 37-42.

Kissling, E., Ellsworth, W. L., Eberhart-Phillips, D., Kradolfer, U., 1994. Initial reference models in local tomography, Journal of Geophysical Research, 99(B10): 19635-19646.

Komatitsch, D., Liu, Q., Tromp, J., Suss, P., Stidham, C., Shaw, J. H., 2004. Simulations of Ground Motion in the Los Angeles Basin Based upon the Spectral-Element Method. Bulletin of the Seismological Society of America, 94(1): 187-206.

Komatitsch, D., Ritsema, J., Tromp, J., 2002. Geophysics: The spectral-element method, beowulf computing, and global seismology. Science, 298(5599): 1737-1742.

Komatitsch, D., Tromp, J., Sciences, P., 1999. Introduction to the spectral element method for three-dimensional seismic wave propagation. Geophysical Journal International, 139(3): 806-822.

Lei, W., Ruan, Y., Bozdağ, E., Peter, D., Lefebvre, M., Komatitsch, D., Tromp, J., Hill, J., Podhorszki, N., Pugmire, D., 2020. Global adjoint tomography-model GLAD-M25. Geophysical Journal International, 223(1): 1-21.

Lee, E.-J., Chen, P., Jordan, T. H., Maechling, P. B., Denolle, M. A. M., Beroza, G. C., 2014. Full-3-D tomography for crustal structure in Southern California based on the scattering-integral and the adjoint-wavefield methods. Journal of Geophysical Research: Solid Earth, 119(8): 6421-6451.

Liu, D. C., Nocedal, J., 1989. On the limited memory BFGS method for large scale optimization. Mathematical Programming, 45(1-3): 503-528.

Liu, Q., Polet, J., Komatitsch, D., Tromp, J., 2004. Spectral-element moment tensor inversions for earthquakes in Southern California. Bulletin of the Seismological Society of America, 94(5): 1748-1761.

Liu, Q., Bin Waheed, U., Borisov, D., Simons, F. J., Gao, F., Williamson, P., 2022. Full-waveform

centroid moment tensor inversion of passive seismic data acquired at the reservoir scale. Geophysical Journal International, 230(3): 1725-1750.
Ma, Y., Hale, D., 2013. Wave-equation reflection traveltime inversion with dynamic warping and full-waveform inversion. Geophysics, 78(6): R223-R233.
MacEira, M., Larmat, C., Porritt, R. W., Higdon, D. M., Rowe, C. A., Allen, R. M., 2015. On the validation of seismic imaging methods: Finite frequency or ray theory?, Geophysical Research Letters, 42(2): 323-330.
McNamara, D. E., Hutt, C. R., Gee, L. S., Benz, H. M., Buland, R. P., 2009. A Method to Establish Seismic Noise Baselines for Automated Station Assessment, Seismological Research Letters, 80(4): 628-637.
McNamara, D. E., Buland, R. P., 2004. Ambient Noise Levels in the Continental United States. Bulletin of the Seismological Society of America, 94(4): 1517-1527.
Métivier, L., Brossier, R., Operto, S., Virieux, J., 2016. Full waveform inversion and the truncated-Newton method. SIAM Journal on Scientific Computing, 35(2): B401-B437.
Modrak, R., Tromp, J., 2016. Seismic waveform inversion best practices: Regional, global and exploration test cases. Geophysical Journal International, 206(3): 1864-1889.
Nakata, N., Chang, J. P., Lawrence, J. F., Boue, P., 2015. Body wave extraction and tomography at Long Beach, California, with ambient-noise interferometry. Journal of Geophysical Research: Solid Earth, 120(2): 1159-1173.
Nakata, N., Boue, P., Brenguier, F., Roux, P., Ferrazzini, V., Campillo, M., 2016. Body and surface wave reconstruction from seismic noise correlations between arrays at Piton de la Fournaise volcano. Geophysical Research Letters, 43(3): 1047-1054.
Operto, S., Gholami, Y., Prieux, V., Ribodetti, A., Brossier, R., Metivier, L., Virieux, J., 2013. A guided tour of multiparameter full-waveform inversion with multicomponent data: From theory to practice. The Leading Edge, 32(9): 1040-1054.
Peter, D., Komatitsch, D., Luo, Y., Martin, R., Le Goff, N., Casarotti, E., Le Loher, P., Magnoni, F., Liu, Q., *et al.,* 2011. Forward and adjoint simulations of seismic wave propagation on fully unstructured hexahedral meshes. Geophysical Journal International, 186(2): 721-739.
Pratt, R. G., 1999. Seismic waveform inversion in the frequency domain, Part 1: Theory and verification in a physical scale model. Geophysics, 64(3): 888-901.
Ren, Z., Liu, Y., 2016. A hierarchical elastic full-waveform inversion scheme based on wavefield separation and the multistep-length approach. Geophysics, 81(3): 99-123.
Riahi, A., Shomali, Z-H., Obermann, A., Kamayestani, A., 2021. Simultaneous retrieval of body and surface waves in the Dehdasht area, Iran, from the seismic ambient field and the observation of spurious artefacts. Geophysical Journal International, 227(2): 1193-1203.
Rickett, J. E., 2003. Illumination-based normalization for wave-equation depth migration. Geophysics, 68(4): 1371-1379.
Salinas, V., Ugalde, A., Kamayestani, A., Jokar, M., Gharibvand, M. M., Villasenor, A., Heidari G., 2019. Designing and testing a network of passive seismic surveying and monitoring in Dehdasht (South Western Iran). Geophysical Prospecting, 67(6): 1652-1663.
Sherkati, S., Molinaro, M., de Lamotte, D. F., Letouzey, J., 2005. Detachment folding in the Central and Eastern Zagros fold-belt (Iran): Salt mobility, multiple detachments and late basement control. Journal of Structural Geology, 27(9): 1680-1696.
Shin, C., Jang, S., Min, D.-J., 2001. Improved amplitude preservation for prestack depth migration by inverse scattering theory. Geophysical Prospecting, 49(5): 592-606.
Shomali, Z., Kamayestani, A., Heidari, G., 2018. Hydrocarbon Exploration Using High Resolution Local Passive Seismic Tomography ; An application to the Dehdasht region , south-west Iran. In: Proceedings of the 18th Iranian Geophysical Conference: 646-649.
Sirgue, L., Pratt, R. G., 2004. Efficient waveform inversion and imaging: A strategy for selecting temporal frequencies. Geophysics, 69(1): 231-248.
Spetzler, J., Snieder, R., 2004. The Fresnel volume and transmitted waves. Geophysics, 69(3): 653-663.
Tao, K., Grand, S. P., Niu, F., 2017. Full-waveform inversion of triplicated data using a normalized-correlation-coefficient-based misfit function. Geophysical Journal International, 210(3): 1517-1524.
Tape, C., Liu, Q., Maggi, A., Tromp, J., 2009. Adjoint tomography of the southern california crust. Science, 325(5943): 988-992.

Tape, C., Liu, Q., Maggi, A., Tromp, J., 2010. Seismic tomography of the southern California crust based on spectral-element and adjoint methods Geophysical Journal International, 180(1): 433-462.
Tarantola, A., 1984. Inversion of seismic reflection data in the acoustic approximation. Geophysics, 49(8): 1259-1266.
Tarantola, A., 1987. Inverse problem theory : methods for data fitting and model parameter estimation. Elsevier.
Tromp, J., Komatitsch, D., Liu, Q., 2008. Spectral-element and adjoint methods in seismology. Communications in Computational Physics, 3(1): 1-32.
Tselentis, G.A., Serpetsidaki, A., Martakis, N., Sokos, E., Paraskevopoulos, P., Kapotas, S., 2007. Local high-resolution passive seismic tomography and Kohonen neural networks - Application at the Rio-Antirio Strait, central Greece. Geophysics, 72(4): 93-106.
Tselentis, G.-A., Martakis, N., Paraskevopolous, P., Lois, A., 2011. High-resolution passive seismic tomography for 3D velocity, Poisson's ratio ν , and P-wave quality Q_P in the Delvina hydrocarbon field, southern Albania. Geophysics, 76(3): 89-112.
Virieux, J., Asnaashari, A., Brossier, R., Metivier, L., Ribodetti, A., Zhou, W., 2014. An introduction to full waveform inversion. Geophysical References Series: 1-40.
Virieux, J., Operto, S., 2009. An overview of full-waveform inversion in exploration geophysics. Geophysics, 74(6): WCC1-WCC26.
Wu, R., Toksöz, M. N., 1987. Diffraction tomography and multisource holography applied to seismic imaging. Geophysics, 52(1): 11-25.